Intermediate-magnitude postseismic slip follows intermediate-magnitude (M 4 to 5) earthquakes in California

M. A. Alwahedi[1,2], J. C. Hawthorne[3]

[1]School of Earth and Environment, University of Leeds, Leeds, UK
[2]Now at Institute for Risk and Disaster Reduction, University College London, London, UK
[3]Department of Earth Sciences, University of Oxford, Oxford, UK

Key Points:

- We examine postseismic slip following M4-5 earthquakes using borehole strain data
- The median estimated postseismic moment is 0.4 times the coseismic moment
- The postseismic moment ratio is intermediate between estimates for small and large earthquakes

Corresponding author: J. C. Hawthorne, `jessica.hawthorne@earth.ox.ac.uk`

Abstract

The magnitude of postseismic slip is useful for constraining physical models of fault slip. Here we examine the postseismic slip following intermediate-magnitude (M 4 to 5) earthquakes by systematically analyzing data from borehole strainmeters in central and northern California. We assess the noise in the data and identify 36 records from 12 earthquakes that can be interpreted. We estimate postseismic to coseismic moment ratios by comparing the coseismic strain changes with strain changes induced by afterslip in the following 1.5 days. The median estimated postseismic moment is 0.36 times the coseismic moment, with a 90% confidence interval between 0.22 and 0.54. This postseismic moment is slightly larger than typically observed following large ($M > 6$) earthquakes but smaller than observed following small (M 2 to 4) earthquakes. The intermediate-magnitude postseismic slip suggests a size dependence in the dynamics of earthquakes or in the properties of fault areas that surround earthquakes.

1 Introduction

Deformation in the hours to years following earthquakes accumulates via a range of processes, including afterslip, poroelastic flow, and viscoelastic deformation. Afterslip is usually the largest cause of deformation in the first few hours to months. The afterslip that accumulates following large ($M > 6$) earthquakes typically has moment equal to 10 to 30% of the coseismic moment (e.g., Cetin et al., 2012; D'Agostino, Cheloni, Fornaro, Giuliani, & Reale, 2012; Donnellan & Lyzenga, 1998; Gahalaut et al., 2008; Gonzalez-Ortega et al., 2014; Johanson & Bürgmann, 2010; Lin et al., 2013; Segall, Bürgmann, & Matthews, 2000), though afterslip moments for individual earthquakes range from a few percent to several hundred percent of the coseismic moment (see Figure 4, Bürgmann et al. (2001); Dogan et al. (2014); Freed (2007); Langbein, Murray, and Snyder (2006); Paul, Lowry, Bilham, Sen, and Smalley (2007)).

While afterslip moments vary, the postseismic to coseismic moment ratios estimated for large earthquakes show no systematic trend with magnitude (see Lin et al. (2013), Fattahi, Amelung, Chaussard, and Wdowinski (2015), and Figure 4 for summaries). The inferred magnitude-independent afterslip is consistent with a self-similar model of earthquakes, where large events are scaled versions of smaller ones. However, large afterslip following small earthquakes has been proposed to explain the long recurrence intervals of small repeating earthquakes (Chen & Lapusta, 2009), and analysis of small (M 1.9 to 3.5) earthquakes near San Juan Bautista, CA revealed that those small earthquakes had afterslip with moment roughly equal to the coseismic moment, on average (Hawthorne, Simons, & Ampuero, 2016). Those large afterslip moments could simply indicate that the frictional properties of the San Andreas Fault near San Juan Bautista region are unusual, and more prone to large afterslip. Afterslip with moment 1.5 to 3 times the coseismic moment was identified following several larger earthquakes in the area: the 2004 M 6 Parkfield earthquake (Barbot, Fialko, & Bock, 2009; Freed, 2007; Langbein et al., 2006), the 2007 M 5.4 Alum Rock earthquake (Murray-Moraleda & Simpson, 2009), and the 1998 M 5.1 San Juan Bautista earthquake (Taira, Bürgmann, Nadeau, & Dreger, 2014).

But the large afterslip moments identified following $M < 3.5$ earthquakes could also indicate that small earthquakes generally behave differently—that the self-similar scaling of postseismic slip breaks down as earthquakes become smaller. For example, the afterslip moment could change as earthquake rupture extents become smaller than the seismogenic zone width, so that most afterslip occurs within the seismogenic zone, rather than above and below it. Or the afterslip moment could change as earthquake rupture extents become similar to the minimum earthquake nucleation size, and thus become too small to drive more rapid slip (Chen & Lapusta, 2009).

In this study, we further examine how afterslip moment varies with earthquake size by examining intermediate-magnitude (M 4 to 5) earthquakes. Only a few afterslip moments have been estimated for M 4 to 6 earthquakes, and all reported values are large. Afterslip moments between 1 and 5 times the coseismic moment were observed following M 4.7 to 5.5 earthquakes on the Chaman fault (Furuya & Satyabala, 2008), on the Ghazaband fault (Fattahi et al., 2015), near Alum Rock, CA (Murray-Moraleda & Simpson, 2009), and near Mogul, NV (Bell, Amelung, & Henry, 2012). However, these large afterslip moments could reflect a reporting bias, as smaller amounts of afterslip would be difficult to observe.

Here we use high-precision borehole strain data to examine postseismic slip following M 4 to 5 earthquakes in central and northern California. We systematically identify earthquakes with resolvable coseismic deformation at each of 12 strainmeters in the PBO and USGS networks. We are able to assess the afterslip moment with reasonable accuracy for 12 earthquakes. The median afterslip moment is roughly 0.4 times the coseismic moment, between the values obtained for smaller and larger earthquakes.

2 Available Data and Earthquakes

We examine data from 12 strainmeters located along the San Andreas Fault in California, shown in Figure 1. More than half of the high-quality earthquake records will come from strainmeter SJT, which was installed by the USGS in 1983 at the northern end of the central creeping section of the San Andreas Fault Gladwin, Gwyther, Hart, Francis, and Johnston (1987). The remaining records come from strainmeters that were installed by UNAVCO as part of the Plate Boundary Observatory (PBO). We consider data from 11 PBO strainmeters installed between 2006 and 2008. Strainmeters B073, B075, B076, B078, and B079 are located near Parkfield, at the southern edge of the central creeping section, while strainmeters B058, B065, and B067 are located near San Juan Bautista, at the northern edge of the central creeping section, and strainmeters B045, B934, and B935 are located close to the Mendecino triple junction, near another creeping section of the San Andreas.

Small earthquakes occur frequently along these creeping sections, mostly at depths of 4 to 15 km (e.g., Irwin & Barnes, 1975; Waldhauser & Schaff, 2008). We begin our analysis by identifying all M 4 to 6 earthquakes that occurred within 30 km of the strainmeters while the strainmeters were operating, as recorded in the NCSN catalog. This identification recovers 112 potential earthquake-station pairs, or 112 potential earthquake records. But we will find that only 14 records, which cover 12 unique earthquakes, have low enough noise level that we can usefully assess the magnitude of afterslip.

3 Initial Data Processing

The deformation produced by co- and postseismic slip are recorded at the strainmeters via three to four horizontal extensometers, which are located at depths of 150 to 250 m and measure changes in the horizontal borehole width at various azimuths. SJT records deformation at 18-minute intervals, and we use 10-minute data from the PBO strainmeters. We convert the time-varying extensometer measurements to the three time-varying horizontal components of strain ε_{E+N}, ε_{E-N}, and ε_{2EN} using the tidal calibrations derived by J. Langbein for strainmeter SJT and by Hodgkinson, Langbein, Henderson, Mencin, and Borsa (2013) for the PBO strainmeters.

We will directly analyze the time series of ε_{E+N}, ε_{E-N}, and ε_{2EN} recorded at strainmeter SJT. But for the PBO strainmeters, we analyze different linear combinations of these strain components. All the strain components are recorded with high instrumental precision, less than 1 nanostrain. But the various components of strain have different sensitivity to atmospheric and hydrologic noise. So we follow the approach of Hawthorne,

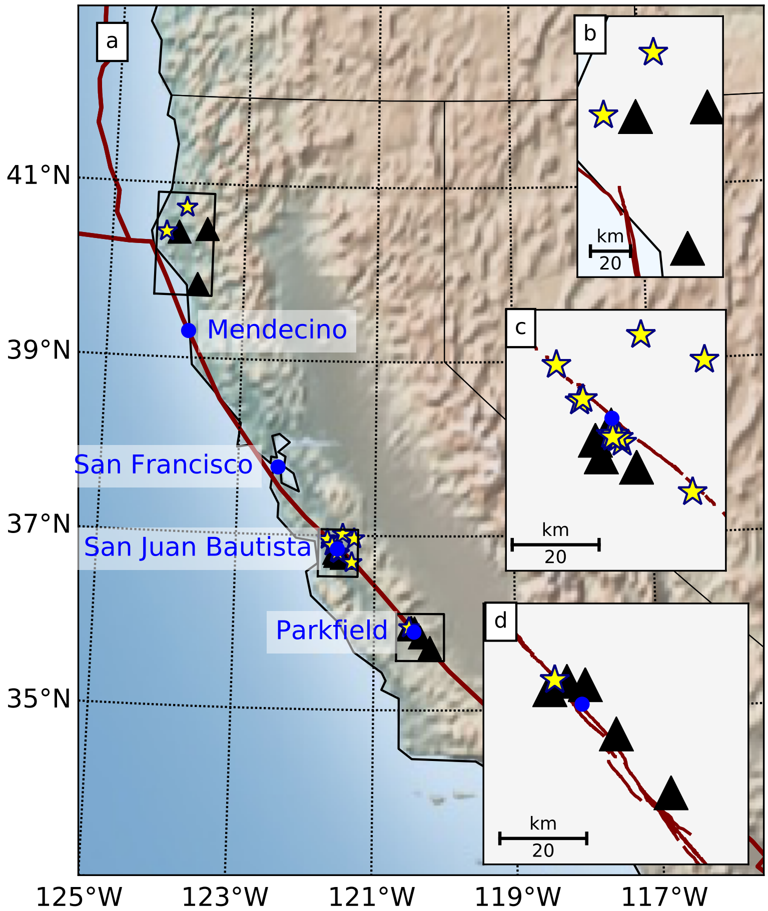

Figure 1. (a) Map of the central San Andreas Fault system in California. In all plots, black triangles are strainmeter locations, yellow stars are the earthquakes for which we estimate post-seismic signals, blue circles are cities, and the red lines mark the plate boundary. (b), (c), and (d) Maps of the three clusters of strainmeters. The strainmeters in each panel are, from west to east, (b) B045, B934, and B935; (c) B058, B067, SJT, and B065; (d) B075, B073, B076, B078, and B079. Note that the marker for SJT is behind the central group of earthquakes in panel c.

Bostock, Royer, and Thomas (2016) to identify linear combinations of ε_{E+N}, ε_{E-N}, and ε_{2EN} that are normally less noisy: the components that have minimal response to atmospheric pressure variations. We refer to the linear combinations that are closest to the original components as ε_{E+N-na}, ε_{E-N-na}, and ε_{2EN-na}, and we will analyze all three time series at the PBO strainmeters, though we note that only two of these three components are independent. The third component is a linear combination of the first two.

Having isolated the strain components of interest, we estimate and remove several non-tectonic signals from each time series, following, for example, Hart, Gladwin, Gwyther, Agnew, and Wyatt (1996); Langbein (2010); Roeloffs (2010), and Hawthorne, Bostock, et al. (2016). To remove borehole curing signals, we discard the first 18 months of data at each station and then fit and remove a linear trend and a decaying exponential with time constant around 1 year. Then we estimate and remove shorter-timescale nontectonic variations. We compare the tidal model of Cartwright and Edden (1973) with the data and identify tidal frequencies that are likely to have tidal signals with amplitudes of at least 0.5 times the noise level. We estimate best-fitting sinusoids at those frequencies and remove them. At SJT, we also estimate and remove a linear response to atmospheric pressure and a periodic 3-hour signal that is likely instrumental noise, as identified by Hawthorne, Simons, and Ampuero (2016).

4 Interpreting Example Strain Records

After removing these non-tectonic signals, we can analyze the earthquake- and afterslip-induced strain. Several examples of the co- and postseismic strain are shown in Figures 2 and S1-S18. Figure 2a shows a high quality record of a M 4.2 earthquake located about 5 km NE of strainmeter B067. An abrupt coseismic strain step is followed by the gradual accumulation of postseismic strain over the two days shown. Figure 2b shows a similar record of a M 4.0 earthquake located about 5 km SE of strainmeter SJT, but here the signal to noise ratio is lower.

In our modelling, we will assume that the postseismic strain is created by afterslip. If afterslip occurs in an area within 1 to 2 earthquake radii of the earthquake rupture, as is usually observed following large earthquakes (D'Agostino et al., 2012; Ryder, Parsons, Wright, & Funning, 2007), and if the earthquake radius is small relative to the earthquake-strainmeter distance, then the co- and postseismic slip should appear co-located from the perspective of the strain observations. In other words, the co- and postseismic slip should have approximately the same Green's functions. Such similar Green's functions are consistent with the data in Figure 2. The ratio of postseismic to coseismic strain is similar on the three strain components, as expected if the strains are given by multiplying the co- and postseismic moments by the same Green's functions.

In this study, we are interested in the ratio of the postseismic moment to the coseismic moment. If the Green's functions are the same, the moment ratio can be obtained simply by dividing the postseismic strain by the coseismic strain. In Figure 2a, for instance, we may note that the postseismic strains accumulated within 2 days of the earthquake have magnitude about 20% of the amplitude of the coseismic strains. Such strain ratios suggest that the afterslip moment accumulated within 2 days of the earthquake is equal to about 20% of the coseismic moment.

5 Identifying Interpretable Strain Records

Our search for earthquakes within 30 km of the strainmeters revealed 112 potential earthquake records. But most of these are not interpretable. First, many are too noisy. In our initial culling of the data, we visually examine the 112 earthquake records and retain only those where the coseismic offset is well resolved on at least one component.

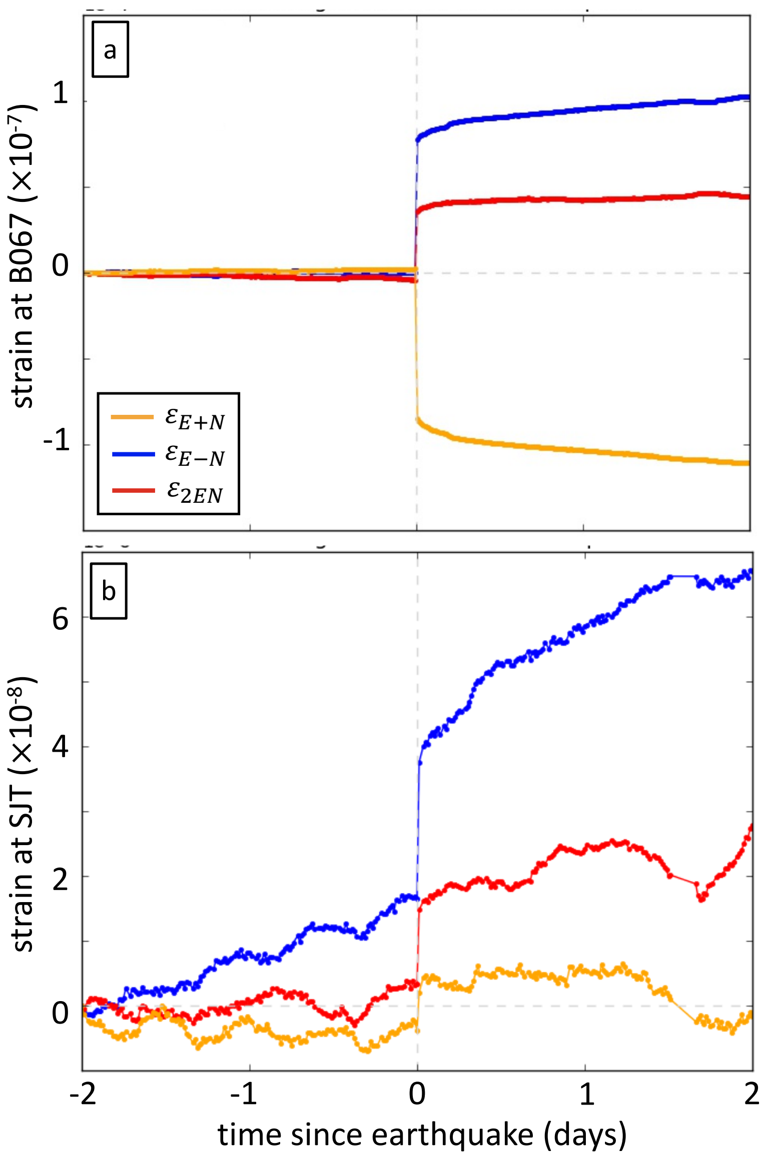

Figure 2. Illustrative records of co- and postseismic strain for (a) a M 4.2 earthquake on 20-Nov-2015, recorded at B067 and located 5 km NE of the strainmeter at 6 km depth and (b) a M 4.0 earthquake on 11-Feb-2001, recorded at SJT and located 5 km SE of the strainmeter at 6 km depth.

This selection does not bias our analysis toward small postseismic to coseismic moment ratios because the noise in the strain data has a random walk character (Hawthorne & Rubin, 2013; Langbein & Johnson, 1997). The uncertainty in the postseismic strain accumulation, which occurs over a few days, is larger than the uncertainty in the coseismic strain accumulation. For the postseismic strain to be resolvable when the coseismic strain is not, it would have to be about 10 times larger than the coseismic strain.

We do not analyze all records with well-resolved coseismic offsets, however. Some are too complex to interpret because they occur within earthquake clusters or because they trigger creep events. Creep events on the shallow San Andreas Fault are mostly hours- to days-long intervals when part of the fault accelerates to rates of order mm to cm per hour (Bilham, Suszek, & Pinkney, 2004; Gladwin, Gwyther, Hart, & Breckenbridge, 1994; S. Schulz, Burford, & Mavko, 1983; S. S. Schulz, 1989; Thurber & Sessions, 1998). In principle, creep events triggered by earthquakes can be classified as afterslip (e.g., Floyd et al., 2016; Fukuda, Johnson, Larson, & Miyazaki, 2009; Langbein et al., 2006). We choose to exclude creep events from our analysis for two reasons. First, it is unclear whether the fault zone processes that create triggered creep events are the same as the processes that usually create afterslip. The spontaneous occurrence of creep events suggest a partially slip rate-weakening rheology that drives acceleration (e.g., Belardinelli, 1997; Wei, Kaneko, Liu, & McGuire, 2013) while afterslip is often modeled with a slip rate-strengthening rheology, so that increased slip rates are driven exclusively by the imposed coseismic stress (Helmstetter & Shaw, 2009; Marone, Scholtz, & Bilham, 1991; Perfettini & Avouac, 2004).

Second, and more importantly, we exclude creep events because it is difficult to estimate their moments. As noted above, we can estimate the relative moment of afterslip that is located close to the coseismic slip simply by computing the ratio of the postseismic to coseismic strain. But to estimate the relative moment of the triggered creep events, we would need to account for the difference in Green's functions between the coseismic rupture and the creep event slip. And we do not know the creep event locations or the coseismic Green's functions well enough to account for that difference. So we identify creep events by (1) looking at the nearby surface USGS creepmeter records and (2) examining how the postseismic to coseismic strain ratio varies among the different components of strain. The earthquakes excluded because of noise and nearby creep events are listed in table S1.

6 Estimates of Postseismic Strain

After identifying earthquakes with well-resolved coseismic steps and excluding those with visible creep events, we are left with 18 records, or 18 earthquake-station pairs, which cover 14 independent earthquakes. We will estimate the coseismic and postseismic strain of these earthquakes within a 1.5-day period. But first, we remove a linear trend that may represent seasonal or hydrological variations. We estimate the trend from the strain observations made in the two days before the earthquakes: by dividing the change in strain between 2 days and 5 hours before the earthquake by that time interval (43 hours). We extrapolate the estimated "long-term" strain rate through the co- and postseismic period and subtract it from the strain time series. Note that the offset-over-time approach to determining offsets and trends is appropriate for random walk noise, as appears to characterize the strain data (Hawthorne & Rubin, 2013; Langbein & Johnson, 1997).

After removing the long-term trend, we estimate the coseismic and postseismic strain changes for each of the three strain components. The coseismic strain change is defined as the strain accumulated within the 40-minute interval centered on the earthquake time. This 40-minute coseismic interval allows us to identify the entire coseismic strain step from the 10- to 18-minute data. We interpolate between data points as necessary. The postseismic strain change is defined as the strain that accumulates between 20 minutes and 1.5 days after the earthquake. The 1.5-day interval is chosen as a compromise between signal and noise. It is long enough to allow significant strain to accumulate but is short enough to avoid the large atmospheric and hydrological noise that can accumulate when longer time intervals are considered.

As noted earlier, we take the ratio of the postseismic to coseismic strains on each component as an estimate of ratio of the postseismic to coseismic moments. To assess how well resolved each postseismic moment ratio is, we examine how it would change if noise were added. We randomly pick 3000 4-day-long intervals of the strain time series to use as 3000 realizations of the noise. We add each realization to the strain data of interest, recompute and subtract a long-term trend, extract the coseismic and postseismic strain changes, and compute their ratio. With this approach, we obtain a probability distribution for the postseismic to coseismic moment ratios for each earthquake and component. We identify and will examine the ratios from the earthquakes and components that have reasonably low uncertainty ranges: those where 70% of the estimated ratios fall within a range smaller than 2 (e.g., between 0 and 2, or between 0.5 and 2.5). These ratios and their 70% confidence bounds are listed in table S2 and are plotted in Figure 3a.

Most of the estimated postseismic to coseismic moment ratios cluster between 0 and 1. 64% of them are between 0.2 and 0.6. Note that two earthquakes, a M 4.9 and a M 4.25, appear to have well-resolved but negative moment ratios. Such negative postseismic moment ratios would seem to imply that the fault is slipping backwards. However, the signal from the M 4.9 may simply result from hydrological noise; there was significant rainfall in January 1993, when the earthquake occurred (Figures S3 and S19). The signal from the M 4.25 is well resolved (Figure S10). But its postseismic to coseismic moment ratios are different on the different components, suggesting that the postseismic strain may result from a triggered creep event, or from slip occurring in a different location than the coseismic slip. We choose to keep these two earthquakes in our analysis because we had not excluded them before estimating the collection of moment ratios.

Our goal here is not understand individual events, but to determine the typical afterslip moments of the available M 4 to 5 earthquakes. The median of the estimated postseismic to coseismic moment ratios is 0.31. But it may be more appropriate to take the median over earthquakes, to avoid overweighting a few events that have more than one observation. So we group the estimated moment ratios by earthquake, take the median for each group, and then take the median among the 12 unique earthquakes. The median earthquake-grouped moment ratio is 0.36.

To determine the uncertainty on the median moment ratio, we randomly pick sets of values from the probability distributions for each earthquake and component, which were obtained above by adding various realizations of the noise. We pick 4000 sets of ratios and estimate their earthquake-grouped medians. Figure 3b shows a histogram of these medians, which represents the probability distribution of the median postseismic to coseismic moment ratio. The distribution implies that the median postseismic ratio is between 0.28 and 0.48 with 70% probability and between 0.22 and 0.54 with 90% probability.

7 Discussion and Conclusion

The postseismic to coseismic moment ratios estimated here are plotted along with the ratios inferred for smaller and larger earthquakes in Figures 4 and S20. The postseismic moments for smaller ($M < 3.5$) earthquakes were obtained over the same time interval considered here: from 20 minutes to 1.5 days after the earthquakes (Hawthorne, Simons, & Ampuero, 2016). The postseismic observations of larger earthquakes were made over a range of timescales, from days to years after the earthquakes. Postseismic moment

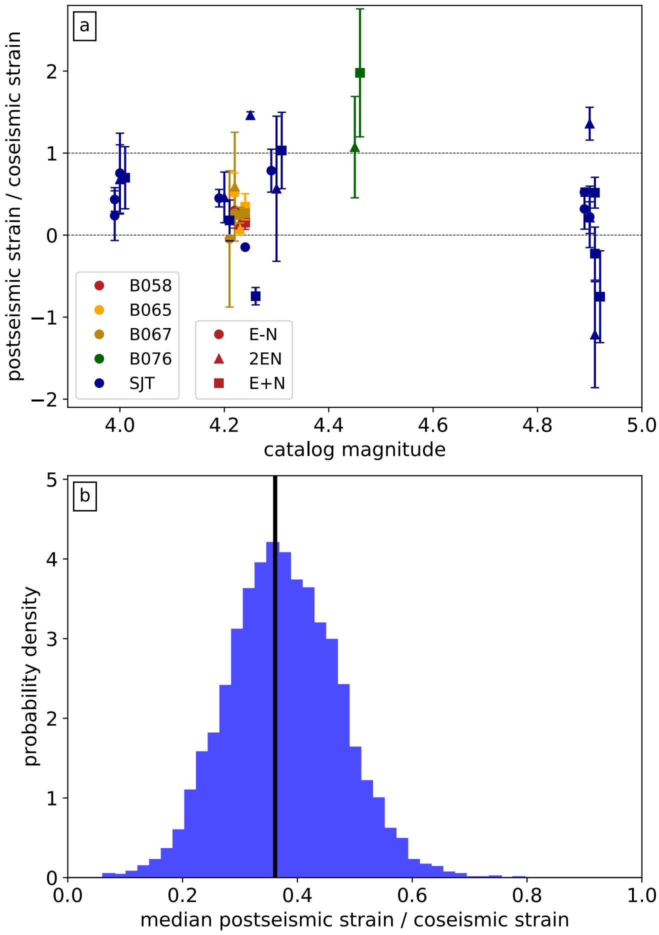

Figure 3. (a) Observed ratios of the postseismic strain changes, from 20 minutes to 1.5 days after the earthquakes, to the coseismic strain changes, from 20 minutes before to 20 minutes after the earthquakes. Each measurement comes from one component at one strainmeter, as indicated by color and symbol. Error bars indicate 70% uncertainty ranges. Note that we randomly shift the magnitudes by up to 0.015 to avoid plotting points on top of each other. (b) Vertical black line: median postseismic to coseismic strain ratio, obtained by taking the median over earthquakes. Probability distribution of the median postseismic to coseismic strain ratio, obtained by considering various realizations of the noise.

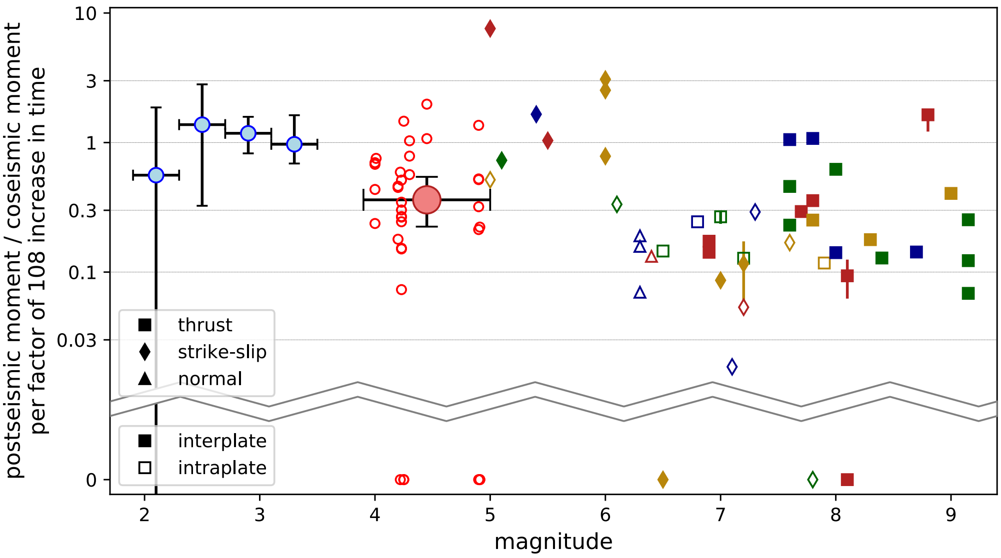

Figure 4. Time-normalized postseismic to coseismic moment ratios for earthquakes with a range of magnitudes. Note that the y-axis is on a log scale but that zero values are plotted below the break. The small red open circles are the individual measurements from this study, and the large red circle with error bars is the event-averaged median with 90% uncertainty ranges vertically and the range of magnitudes horizontally. The blue circles with error bars on the left are the moment ratios obtained by Hawthorne, Simons, and Ampuero (2016) for small earthquakes near San Juan Bautista, again with 90% uncertainty ranges vertically and the range of magnitudes horizontally. The points on the right come from a range of studies of intermediate and large-magnitude earthquakes, as listed in the text.

is often found to accumulate as the logarithm of time after the earthquake, so for a simple comparison in Figure 4, we normalize the larger earthquake observations to represent the moment accumulation expected for factor of 108 (=1.5 days / 15 minutes) increase in time after the earthquake, assuming a logarithmic moment accumulation.

The postseismic to coseismic moment ratios we observe, with median 0.36, is slightly larger than the moment typically seen after large ($M > 6$) earthquakes. Most (though not all) large earthquakes show postseismic moments smaller than 0.3 times the coseismic moment (Amoruso & Crescentini, 2009; Barbot, Hamiel, & Fialko, 2008; Bürgmann et al., 2001; Cetin et al., 2012; Cheloni et al., 2010; Chlieh et al., 2007; D'Agostino et al., 2012; Diao, Wang, Wang, Xiong, & Walter, 2018; Dogan et al., 2014; Floyd et al., 2016; Freed, 2007; Gonzalez-Ortega et al., 2014; Heki, Miyazaki, & Tsuji, 1997; Hobbs, Kyriakopoulos, Newman, Protti, & Yao, 2017; Hsu et al., 2006; Jacobs, Sandwell, Fialko, & Sichoix, 2002; Johanson & Bürgmann, 2010; Jónsson, 2008; Langbein et al., 2006; Lin et al., 2013; Mahsas et al., 2008; Malservisi et al., 2015; Melbourne, Webb, Stock, & Reigber, 2002; Miura, Suwa, Hasegawa, & Nishimura, 2004; Podgorski et al., 2007; Pritchard & Simons, 2006; Rolandone et al., 2018; Ryder, Bürgmann, & Sun, 2010; Ryder et al., 2007; Savage & Svarc, 1997; Segall et al., 2000; Shrivastava et al., 2016; Sreejith et al., 2016; Subarya et al., 2006; Wen, Li, Xu, Ryder, & Bürgmann, 2012). Our M 4 to 5 moment ratios are smaller than the reported moments for M 5 to 6 earthquakes (Barbot et al., 2009; Fattahi et al., 2015; Freed, 2007; Furuya & Satyabala, 2008; Langbein et al., 2006; Murray-Moraleda & Simpson, 2009; Taira et al., 2014). But the high values for M 5 to 6 earthquakes could result from observational bias; smaller postseismic moments may not be reported because they would be harder to observe. More interestingly, then, we note that our M 4 to 5 moment ratios are also smaller than the roughly one to one ratios observed for $M < 3.5$ earthquakes Hawthorne, Simons, and Ampuero (2016).

There are several possible explanations for the observed variation in postseismic moment with magnitude. First, the varying postseismic moments could reflect fault properties. Smaller earthquakes may be more likely to occur on creeping sections of faults, perhaps on asperities surrounded by velocity-strengthening fault sections that are more prone to large postseismic slip (e.g., Rolandone et al., 2018; Vaca, Vallée, Nocquet, Battaglia, & Régnier, 2018). The postseismic moment estimates for $M < 3.5$ earthquakes all come from a single 20-km-wide fault segment near San Juan Bautista, CA, which could have particular properties. But most of the earthquakes investigated here come from that same fault segment, and half are obtained from measurements on the same strainmeter, SJT (see Figures S1 to S10 for the time series).

It seems unlikely that other physical processes create some of the postseismic deformation we observe. Significant viscoelastic deformation is unlikely to accumulate on the brief, 2-day timescale examined here (e.g., Bruhat, Barbot, & Avouac, 2011; Johnson, Bürgmann, & Freymueller, 2009; Pollitz, Banerjee, Burgmann, Hashimoto, & Choosakul, 2006). Poroelastic deformation can accumulate more quickly, but it typically has smaller magnitude, just few percent of the coseismic deformation (Jónsson, Segall, Pedersen, & Björnsson, 2003; Peltzer, Rosen, Rogez, & Hudnut, 1996, 1998) unless there is a nonlinear near-surface response (e.g., Chia, Wang, Chiu, & Liu, 2001; Manga & Wang, 2007; Quilty & Roeloffs, 1997; Wang, Wang, & Manga, 2004) or near-borehole deformation due to shaking (Barbour, Agnew, & Wyatt, 2015), and Hawthorne, Simons, and Ampuero (2016) identified no strong near-surface response to passing seismic waves or to creep events in the San Juan Bautista region or at strainmeter SJT.

Assuming, then, that the postseismic deformation reflects afterslip, the magnitude-dependent moment ratios could reflect the time intervals in which we observe that afterslip. Postseismic moment is often observed to accumulate as log of the time t since the earthquake, or at a rate of $1/t$. But at short times t after the earthquake, the moment rate may be slower than would be predicted by a $1/t$ extrapolation, perhaps because the slipping region is growing outward from the coseismic rupture (Ariyoshi et al., 2009; Dublanchet, Bernard, & Favreau, 2013a, 2013b; Lui & Lapusta, 2016; Perfettini & Ampuero, 2008) or because the fault takes time to accelerate in response to the coseismic stress increase (Marone et al., 1991; Montési, 2004; Perfettini & Avouac, 2004; Savage, 2007).

The coseismic rupture geometry can also influence the magnitude of postseismic slip. Small earthquakes tend to be more circular (e.g., Abercrombie, 1995; Gomberg, Wech, Creager, Obara, & Agnew, 2016; Scholz, 1982; Shaw, 2013), and thus may have a larger perimeter-to-area ratio and a larger region close to the coseismic rupture that can experience and respond to strong coseismic stress changes (Hawthorne, Simons, & Ampuero, 2016). However, the transition from circular to rectangular ruptures is typically inferred to occur when ruptures first start to span the seismogenic zone, at a magnitude around 6 or 7. We observe a change in postseismic moment at a magnitude of 4 to 5.

Alternatively, the magnitude-dependent postseismic moments could reflect a more fundamental property of earthquake dynamics. For instance, Chen and Lapusta (2009) identified large postseismic slip in rate and state friction models of earthquakes occurring on small asperities, on patches that were not much wider than the earthquake nucleation size. The large afterslip arose because portions of the potentially unstable asperities did not rupture in the earthquakes, and instead slipped via aseismic afterslip.

As observations of postseismic slip continue to accumulate, the ratio of postseismic to coseismic moment may become an important constraint on physical models of earthquake rupture. The postseismic moment ratios will complement observations of coseismic stress drops, which are usually found to be magnitude independent, suggesting that earthquakes are self-similar: that large earthquakes are scaled-up small earthquakes. In this study, we have made observations that appear to contradict self-similarity. The median postseismic moment estimated for the 12 well-resolved M 4 to 5 earthquakes is 0.36 (0.22 to 0.54 with 90% probability). This afterslip moment of these intermediate-magnitude moments is intermediate relative to previous observations; it is slightly larger than is typical of $M > 6$ earthquakes and smaller than observed for $M < 3.5$ earthquakes.

Acknowledgments

Strain and creep data for the San Juan Bautista (SJT) station are provided by the United States Geological Survey and are available at http://earthquake.usgs.gov/monitoring/deformation/data/down-load/table.php. The PBO strain data comes from stations operated by UNAVCO for EarthScope and support ed by the National Science Foundation No. EAR-0350028 and EAR-0732947. It can be obtained via IRIS. The Northern California Seismic Network (NCSN) earthquake catalog is provided by the Northern California Earthquake Data Center and the Berkeley Seismological Laboratory (doi: 10.7932/NCEDC). The plotted fault traces come from the Quaternary fault and fold database, provided by the USGS and the California Geological Survey, and are available at http://earthquake.usgs.gov/hazards/qfaults/. The precipitation data used to interpret some records were provided by the National Oceanic and Atmospheric Administration (NOAA), and were accessed from https://www.ncdc.noaa.gov/cdo-web/.

References

Abercrombie, R. E. (1995). Earthquake source scaling relationships from -1 to 5 ML using seismograms recorded at 2.5-km depth. *J. Geophys. Res.*, *100*, 24015–24036. doi: 10.1029/95JB02397

Amoruso, A., & Crescentini, L. (2009). Slow diffusive fault slip propagation following the 6 April 2009 L'Aquila earthquake, Italy. *Geophys. Res. Lett.*, *36*, L24306. doi: 10.1029/2009GL041503

Ariyoshi, K., Hori, T., Ampuero, J.-P., Kaneda, Y., Matsuzawa, T., Hino, R., & Hasegawa, A. (2009). Influence of interaction between small asperities on various types of slow earthquakes in a 3-D simulation for a subduction plate boundary. *Gondwana Res.*, *16*(3-4), 534–544. doi: 10.1016/j.gr.2009.03.006

Barbot, S., Fialko, Y., & Bock, Y. (2009). Postseismic deformation due to the Mw 6.0 2004 Parkfield earthquake: Stress-driven creep on a fault with spatially variable rate-and-state friction parameters. *J. Geophys. Res.*, *114*, B07405. doi: 10.1029/2008JB005748

Barbot, S., Hamiel, Y., & Fialko, Y. (2008). Space geodetic investigation of the coseismic and postseismic deformation due to the 2003 Mw 7.2 Altai earthquake: Implications for the local lithospheric rheology. *J. Geophys. Res.*, *113*, B03403. doi: 10.1029/2007JB005063

Barbour, A. J., Agnew, D. C., & Wyatt, F. K. (2015). Coseismic strains on Plate Boundary Observatory borehole strainmeters in southern California. *Bull. Seis. Soc. Amer.*, *105*(1), 431–444. doi: 10.1785/0120140199

Belardinelli, M. E. (1997). Increase of creep interevent intervals: a conceptual model. *Tectonophysics*, *277*(1-3), 99–107. doi: 10.1016/S0040-1951(97)00080-2

Bell, J. W., Amelung, F., & Henry, C. D. (2012). InSAR analysis of the 2008 Reno-Mogul earthquake swarm: Evidence for westward migration of Walker Lane style dextral faulting. *Geophys. Res. Lett.*, *39*(18), L18306. doi: 10.1029/2012GL052795

Bilham, R., Suszek, N., & Pinkney, S. (2004). California Creepmeters. *Seis. Res. Lett.*, *75*(4), 481–492. doi: 10.1785/gssrl.75.4.481

Bruhat, L., Barbot, S., & Avouac, J.-P. (2011). Evidence for postseismic deformation of the lower crust following the 2004 Mw6.0 Parkfield earthquake. *J. Geophys. Res.*, *116*(B8), B08401. doi: 10.1029/2010JB008073

Bürgmann, R., Kogan, M. G., Levin, V. E., Scholz, C. H., King, R. W., & Steblov, G. M. (2001). Rapid aseismic moment release following the 5 December, 1997 Kronotsky, Kamchatka, Earthquake. *Geophys. Res. Lett.*, *28*(7), 1331–1334. doi: 10.1029/2000GL012350

Cartwright, D. E., & Edden, A. C. (1973). Corrected tables of tidal harmonics. *Geophys. J. Intern.*, *33*(3), 253–264. doi: 10.1111/j.1365-246X.1973.tb03420.x

Cetin, E., Meghraoui, M., Cakir, Z., Akoglu, A. M., Mimouni, O., & Chebbah, M. (2012). Seven years of postseismic deformation following the 2003 Mw 6.8 Zemmouri earthquake (Algeria) from InSAR time series. *Geophys. Res. Lett.*, *39*(10), L10307. doi: 10.1029/2012GL051344

Cheloni, D., D'Agostino, N., D'Anastasio, E., Avallone, A., Mantenuto, S., Giuliani, R., … Fastellini, G. (2010). Coseismic and initial post-seismic slip of the 2009 Mw 6.3 L'Aquila earthquake, Italy, from GPS measurements. *Geophys. J. Intern.*, *181*(3), 1539–1546. doi: 10.1111/j.1365-246X.2010.04584.x

Chen, T., & Lapusta, N. (2009). Scaling of small repeating earthquakes explained by interaction of seismic and aseismic slip in a rate and state fault model. *J. Geophys. Res.*, *114*, B01311. doi: 10.1029/2008JB005749

Chia, Y., Wang, Y.-S., Chiu, J. J., & Liu, C.-W. (2001). Changes of groundwater level due to the 1999 Chi-Chi earthquake in the Choshui River alluvial fan in Taiwan. *Bull. Seis. Soc. Amer.*, *91*(5), 1062–1068. doi: 10.1785/0120000726

Chlieh, M., Avouac, J.-P., Hjorleifsdottir, V., Song, T.-R. A., Ji, C., Sieh, K., … Galetzka, J. (2007). Coseismic slip and afterslip of the great Mw 9.15 Sumatra–Andaman earthquake of 2004. *Bull. Seis. Soc. Amer.*, *97*(1A), S152–S173. doi: 10.1785/0120050631

D'Agostino, N., Cheloni, D., Fornaro, G., Giuliani, R., & Reale, D. (2012). Space-time distribution of afterslip following the 2009 L'Aquila earthquake. *J. Geophys. Res.*, *117*(B2), B02402. doi: 10.1029/2011JB008523

Diao, F., Wang, R., Wang, Y., Xiong, X., & Walter, T. R. (2018). Fault behavior and lower crustal rheology inferred from the first seven years of postseismic

GPS data after the 2008 Wenchuan earthquake. *Earth Planet. Sci. Lett.*, *495*, 202–212. doi: 10.1016/j.epsl.2018.05.020

Dogan, U., Demir, D. Ö., Çakir, Z., Ergintav, S., Ozener, H., Akoğlu, A. M., ... Reilinger, R. (2014). Postseismic deformation following the Mw 7.2, 23 October 2011 Van earthquake (Turkey): Evidence for aseismic fault reactivation. *Geophys. Res. Lett.*, *41*(7), 2334–2341. doi: 10.1002/2014GL059291

Donnellan, A., & Lyzenga, G. A. (1998). GPS observations of fault afterslip and upper crustal deformation following the Northridge earthquake. *J. Geophys. Res.*, *103*(B9), 21285–21297. doi: 10.1029/98JB01487

Dublanchet, P., Bernard, P., & Favreau, P. (2013a). Creep modulation of Omori law generated by a Coulomb stress perturbation in a 3-D rate-and-state asperity model. *J. Geophys. Res.*, *118*(9), 4774–4793. doi: 10.1002/jgrb.50311

Dublanchet, P., Bernard, P., & Favreau, P. (2013b). Interactions and triggering in a 3-D rate-and-state asperity model. *J. Geophys. Res.*, *118*(5), 2225–2245. doi: 10.1002/jgrb.50187

Fattahi, H., Amelung, F., Chaussard, E., & Wdowinski, S. (2015). Coseismic and postseismic deformation due to the 2007 M5.5 Ghazaband fault earthquake, Balochistan, Pakistan. *Geophys. Res. Lett.*, *42*(9), 3305–3312. doi: 10.1002/2015GL063686

Floyd, M. A., Walters, R. J., Elliott, J. R., Funning, G. J., Svarc, J. L., Murray, J. R., ... Wright, T. J. (2016). Spatial variations in fault friction related to lithology from rupture and afterslip of the 2014 South Napa, California, earthquake. *Geophys. Res. Lett.*, *43*(13), 6808–6816. doi: 10.1002/2016GL069428

Freed, A. M. (2007). Afterslip (and only afterslip) following the 2004 Parkfield, California, earthquake. *Geophys. Res. Lett.*, *34*(6), L06312. doi: 10.1029/2006GL029155

Fukuda, J., Johnson, K. M., Larson, K. M., & Miyazaki, S. (2009). Fault friction parameters inferred from the early stages of afterslip following the 2003 Tokachi-oki earthquake. *J. Geophys. Res.*, *114*, B04412. doi: 10.1029/2008JB006166

Furuya, M., & Satyabala, S. P. (2008). Slow earthquake in Afghanistan detected by InSAR. *Geophys. Res. Lett.*, *35*(6), L06309. doi: 10.1029/2007GL033049

Gahalaut, V. K., Jade, S., Catherine, J. K., Gireesh, R., Ananda, M. B., Kumar, P. D., ... Kumar, S. (2008). GPS measurements of postseismic deformation in the Andaman-Nicobar region following the giant 2004 Sumatra-Andaman earthquake. *J. Geophys. Res.*, *113*(B8), B08401. doi: 10.1029/2007JB005511

Gladwin, M. T., Gwyther, R. L., Hart, R., Francis, M., & Johnston, M. J. S. (1987). Borehole tensor strain measurements in California. *J. Geophys. Res.*, *92*(B8), 7981–7988. doi: 10.1029/JB092iB08p07981

Gladwin, M. T., Gwyther, R. L., Hart, R. H. G., & Breckenbridge, K. S. (1994). Measurements of the strain field associated with episodic creep events on the San Andreas fault at San Juan Bautista, California. *J. Geophys. Res.*, *99*, 4559–4565. doi: 10.1029/93JB02877

Gomberg, J., Wech, A., Creager, K., Obara, K., & Agnew, D. (2016). Reconsidering earthquake scaling. *Geophys. Res. Lett.*, *43*(12), 6243–6251. doi: 10.1002/2016GL069967

Gonzalez-Ortega, A., Fialko, Y., Sandwell, D., Alejandro Nava-Pichardo, F., Fletcher, J., Gonzalez-Garcia, J., ... Funning, G. (2014). El Mayor-Cucapah (Mw 7.2) earthquake: Early near-field postseismic deformation from InSAR and GPS observations. *J. Geophys. Res.*, *119*(2), 1482–1497. doi: 10.1002/2013JB010193

Hart, R. H. G., Gladwin, M. T., Gwyther, R. L., Agnew, D. C., & Wyatt, F. K. (1996). Tidal calibration of borehole strain meters: Removing the effects of small-scale inhomogeneity. *J. Geophys. Res.*, *101*(B11), 25553–25571. doi: 10.1029/96JB02273

Hawthorne, J. C., Bostock, M. G., Royer, A. A., & Thomas, A. M. (2016).

Variations in slow slip moment rate associated with rapid tremor reversals in Cascadia. *Geochem., Geophys., Geosyst.*, *17*(12), 4899–4919. doi: 10.1002/2016GC006489

Hawthorne, J. C., & Rubin, A. M. (2013). Short-time scale correlation between slow slip and tremor in Cascadia. *J. Geophys. Res.*, *118*(3), 1316–1329. doi: 10.1002/jgrb.50103

Hawthorne, J. C., Simons, M., & Ampuero, J.-P. (2016). Estimates of aseismic slip associated with small earthquakes near San Juan Bautista, CA. *J. Geophys. Res.*, *121*(11), 8254-8275. doi: 10.1002/2016JB013120

Heki, K., Miyazaki, S., & Tsuji, H. (1997). Silent fault slip following an interplate thrust earthquake at the Japan Trench. *Nature*, *386*(6625), 595–598. doi: 10.1038/386595a0

Helmstetter, A., & Shaw, B. E. (2009). Afterslip and aftershocks in the rate-and-state friction law. *J. Geophys. Res.*, *114*, B01308. doi: 10.1029/2007JB005077

Hobbs, T. E., Kyriakopoulos, C., Newman, A. V., Protti, M., & Yao, D. (2017). Large and primarily updip afterslip following the 2012 Mw 7.6 Nicoya, Costa Rica, earthquake. *J. Geophys. Res.*, *122*(7), 5712-5728. doi: 10.1002/2017JB014035

Hodgkinson, K., Langbein, J., Henderson, B., Mencin, D., & Borsa, A. (2013). Tidal calibration of Plate Boundary Observatory borehole strainmeters. *J. Geophys. Res.*, *118*(1), 447–458. doi: 10.1029/2012JB009651

Hsu, Y.-J., Simons, M., Avouac, J.-P., Galetzka, J., Sieh, K., Chlieh, M., … Bock, Y. (2006). Frictional afterslip following the 2005 Nias-Simeulue earthquake, Sumatra. *Science*, *312*(5782), 1921–1926. doi: 10.1126/science.1126960

Irwin, W. P., & Barnes, I. (1975). Effect of geologic structure and metamorphic fluids on seismic behavior of the San Andreas fault system in central and northern California. *Geology*, *3*(12), 713–716. doi: 10.1130/0091-7613(1975)3⟨713:EOGSAM⟩2.0.CO;2

Jacobs, A., Sandwell, D., Fialko, Y., & Sichoix, L. (2002). The 1999 (Mw 7.1) Hector Mine, California, earthquake: near-field postseismic deformation from ERS interferometry. *Bull. Seis. Soc. Amer.*, *92*(4), 1433–1442. doi: 10.1785/0120000908

Johanson, I. A., & Bürgmann, R. (2010). Coseismic and postseismic slip from the 2003 San Simeon earthquake and their effects on backthrust slip and the 2004 Parkfield earthquake. *J. Geophys. Res.*, *115*(B7), B07411. doi: 10.1029/2009JB006599

Johnson, K. M., Bürgmann, R., & Freymueller, J. T. (2009). Coupled afterslip and viscoelastic flow following the 2002 Denali Fault, Alaska earthquake. *Geophys. J. Intern.*, *176*(3), 670–682. doi: 10.1111/j.1365-246X.2008.04029.x

Jónsson, S. (2008). Importance of post-seismic viscous relaxation in southern Iceland. *Nat. Geosci.*, *1*(2), 136–139. doi: 10.1038/ngeo105

Jónsson, S., Segall, P., Pedersen, R., & Björnsson, G. (2003). Post-earthquake ground movements correlated to pore-pressure transients. *Nature*, *424*(6945), 179–183. doi: 10.1038/nature01776

Langbein, J. (2010). Computer algorithm for analyzing and processing borehole strainmeter data. *Computers & Geosciences*, *36*(5), 611–619. doi: 10.1016/j.cageo.2009.08.011

Langbein, J., & Johnson, H. (1997). Correlated errors in geodetic time series: Implications for time-dependent deformation. *J. Geophys. Res.*, *102*(B1), 591–603. doi: 199710.1029/96JB02945

Langbein, J., Murray, J. R., & Snyder, H. A. (2006). Coseismic and initial postseismic deformation from the 2004 Parkfield, California, earthquake, observed by global positioning system, electronic distance meter, creepmeters, and borehole strainmeters. *Bull. Seis. Soc. Amer.*, *96*(4B), S304–S320. doi: 10.1785/0120050823

Lin, Y.-n. N., Sladen, A., Ortega-Culaciati, F., Simons, M., Avouac, J.-P., Fielding, E. J., … Socquet, A. (2013). Coseismic and postseismic slip associated with the 2010 Maule Earthquake, Chile: Characterizing the Arauco Peninsula barrier effect. *J. Geophys. Res.*, *118*(6), 3142–3159. doi: 10.1002/jgrb.50207

Lui, S. K. Y., & Lapusta, N. (2016). Repeating microearthquake sequences interact predominantly through postseismic slip. *Nat. Comm.*, *7*, ncomms13020. doi: 10.1038/ncomms13020

Mahsas, A., Lammali, K., Yelles, K., Calais, E., Freed, A. M., & Briole, P. (2008). Shallow afterslip following the 2003 May 21, Mw= 6.9 Boumerdes earthquake, Algeria. *Geophys. J. Intern.*, *172*(1), 155–166. doi: 10.1111/j.1365-246X.2007.03594.x

Malservisi, R., Schwartz, S. Y., Voss, N., Protti, M., Gonzalez, V., Dixon, T. H., … Voyenko, D. (2015). Multiscale postseismic behavior on a megathrust: The 2012 Nicoya earthquake, Costa Rica. *Geochem., Geophys., Geosyst.*, *16*(6), 1848–1864. doi: 10.1002/2015GC005794

Manga, M., & Wang, C.-Y. (2007). Earthquake hydrology. In Hiroo Kanamori & G. Schubert (Eds.), *Treatise on Geophysics* (Vol. 4: Earthquake Seismology, p. 6054). Amsterdam: Elsevier.

Marone, C. J., Scholtz, C. H., & Bilham, R. (1991). On the mechanics of earthquake afterslip. *J. Geophys. Res.*, *96*(B5), 8441–8452. doi: 10.1029/91JB00275

Melbourne, T. I., Webb, F. H., Stock, J. M., & Reigber, C. (2002). Rapid postseismic transients in subduction zones from continuous GPS. *J. Geophys. Res.*, *107*(B10), 2241. doi: 10.1029/2001JB000555

Miura, S., Suwa, Y., Hasegawa, A., & Nishimura, T. (2004). The 2003 M8.0 Tokachi-Oki earthquake – How much has the great event paid back slip debts? *Geophys. Res. Lett.*, *31*(5), L05613. doi: 10.1029/2003GL019021

Montési, L. G. J. (2004). Controls of shear zone rheology and tectonic loading on postseismic creep. *J. Geophys. Res.*, *109*(B10), B10404. doi: 10.1029/2003JB002925

Murray-Moraleda, J. R., & Simpson, R. W. (2009). Geodetically inferred coseismic and postseismic slip due to the M 5.4 31 October 2007 Alum Rock earthquake. *Bull. Seis. Soc. Amer.*, *99*(5), 2784–2800. doi: 10.1785/0120090017

Paul, J., Lowry, A. R., Bilham, R., Sen, S., & Smalley, R. (2007). Postseismic deformation of the Andaman Islands following the 26 December, 2004 Great Sumatra-Andaman earthquake. *Geophys. Res. Lett.*, *34*, L19309. doi: 10.1029/2007GL031024

Peltzer, G., Rosen, P., Rogez, F., & Hudnut, K. (1996). Postseismic rebound in fault step-overs caused by pore fluid flow. *Science*, *273*(5279), 1202–1204. doi: 10.1126/science.273.5279.1202

Peltzer, G., Rosen, P., Rogez, F., & Hudnut, K. (1998). Poroelastic rebound along the Landers 1992 earthquake surface rupture. *J. Geophys. Res.*, *103*(B12), 30131–30145. doi: 10.1029/98JB02302

Perfettini, H., & Ampuero, J. P. (2008). Dynamics of a velocity strengthening fault region: Implications for slow earthquakes and postseismic slip. *J. Geophys. Res.*, *113*, B09411. doi: 10.1029/2007JB005398

Perfettini, H., & Avouac, J. P. (2004). Postseismic relaxation driven by brittle creep: A possible mechanism to reconcile geodetic measurements and the decay rate of aftershocks, application to the Chi-Chi earthquake, Taiwan. *J. Geophys. Res.*, *109*, B02304. doi: 10.1029/2003JB002488

Podgorski, J., Hearn, E. H., McClusky, S., Reilinger, R., Taymaz, T., Tan, O., … Nadariya, M. (2007). Postseismic deformation following the 1991 Racha, Georgia, earthquake. *Geophys. Res. Lett.*, *34*(4), L04310. doi: 10.1029/2006GL028477

Pollitz, F. F., Banerjee, P., Burgmann, R., Hashimoto, M., & Choosakul, N. (2006). Stress changes along the Sunda trench following the 26 December 2004

Sumatra-Andaman and 28 March 2005 Nias earthquakes. *Geophys. Res. Lett.*, *33*(6), L06309. doi: 10.1029/2005GL024558
Pritchard, M. E., & Simons, M. (2006). An aseismic slip pulse in northern Chile and along-strike variations in seismogenic behavior. *J. Geophys. Res.*, *111*, B08405. doi: 10.1029/2006JB004258
Quilty, E. G., & Roeloffs, E. A. (1997). Water-level changes in response to the 20 December 1994 earthquake near Parkfield, California. *Bull. Seis. Soc. Amer.*, *87*(2), 310–317.
Roeloffs, E. (2010). Tidal calibration of Plate Boundary Observatory borehole strainmeters: Roles of vertical and shear coupling. *J. Geophys. Res.*, *115*, B06405. doi: 10.1029/2009JB006407
Rolandone, F., Nocquet, J.-M., Mothes, P. A., Jarrin, P., Vallée, M., Cubas, N., … Font, Y. (2018). Areas prone to slow slip events impede earthquake rupture propagation and promote afterslip. *Science Advances*, *4*(1), eaao6596. doi: 10.1126/sciadv.aao6596
Ryder, I., Bürgmann, R., & Sun, J. (2010). Tandem afterslip on connected fault planes following the 2008 Nima-Gaize (Tibet) earthquake. *J. Geophys. Res.*, *115*(B3), B03404. doi: 10.1029/2009JB006423
Ryder, I., Parsons, B., Wright, T. J., & Funning, G. J. (2007). Post-seismic motion following the 1997 Manyi (Tibet) earthquake: InSAR observations and modelling. *Geophys. J. Intern.*, *169*(3), 1009–1027. doi: 10.1111/j.1365-246X.2006.03312.x
Savage, J. C. (2007). Postseismic relaxation associated with transient creep rheology. *J. Geophys. Res.*, *112*, B05412. doi: 10.1029/2006JB004688
Savage, J. C., & Svarc, J. L. (1997). Postseismic deformation associated with the 1992 Mw 7.3 Landers earthquake, southern California. *J. Geophys. Res.*, *102*(B4), 7565–7577. doi: 10.1029/97JB00210
Scholz, C. H. (1982). Scaling laws for large earthquakes: Consequences for physical models. *Bull. Seis. Soc. Amer.*, *72*(1), 1–14.
Schulz, S., Burford, R. O., & Mavko, B. (1983). Influence of seismicity and rainfall on episodic creep on the San Andreas Fault System in central California. *J. Geophys. Res.*, *88*(B9), 7475–7484. doi: 10.1029/JB088iB09p07475
Schulz, S. S. (1989). *Catalog of creepmeter measurements in California from 1966 through 1988* (Tech. Rep. No. 89-650). USGS. (Version 1.1)
Segall, P., Bürgmann, R., & Matthews, M. (2000). Time-dependent triggered afterslip following the 1989 Loma Prieta earthquake. *J. Geophys. Res.*, *105*(B3), 5615–5634. doi: 10.1029/1999JB900352
Shaw, B. E. (2013). Earthquake surface slip-length data is fit by constant stress drop and is useful for seismic hazard analysis. *Bull. Seis. Soc. Amer.*, *103*(2A), 876–893. doi: 10.1785/0120110258
Shrivastava, M. N., González, G., Moreno, M., Chlieh, M., Salazar, P., Reddy, C. D., … de la Llera, J. C. (2016). Coseismic slip and afterslip of the 2015 Mw 8.3 Illapel (Chile) earthquake determined from continuous GPS data. *Geophys. Res. Lett.*, *43*(20), 2016GL070684. doi: 10.1002/2016GL070684
Sreejith, K. M., Sunil, P. S., Agrawal, R., Saji, A. P., Ramesh, D. S., & Rajawat, A. S. (2016). Coseismic and early postseismic deformation due to the 25 April 2015, Mw 7.8 Gorkha, Nepal, earthquake from InSAR and GPS measurements. *Geophys. Res. Lett.*, *43*(7), 2016GL067907. doi: 10.1002/2016GL067907
Subarya, C., Chlieh, M., Prawirodirdjo, L., Avouac, J. P., Bock, Y., Sieh, K., … McCaffrey, R. (2006). Plate-boundary deformation associated with the great Sumatra-Andaman earthquake. *Nature*, *440*(7080), 46–51. doi: 10.1038/nature04522
Taira, T., Bürgmann, R., Nadeau, R. M., & Dreger, D. S. (2014). Variability of fault slip behavior along the San Andreas Fault in the San Juan Bautista Region. *J. Geophys. Res.*, *119*(12), 8827–8844. doi: 10.1002/2014JB011427

Thurber, C., & Sessions, R. (1998). Assessment of creep events as potential earthquake precursors: application to the creeping section of the San Andreas Fault, California. *Pure Appl. Geophys.*, *152*, 685–705. doi: 10.1007/s000240050172

Vaca, S., Vallée, M., Nocquet, J.-M., Battaglia, J., & Régnier, M. (2018). Recurrent slow slip events as a barrier to the northward rupture propagation of the 2016 Pedernales earthquake (Central Ecuador). *Tectonophysics*, *724-725*, 80–92. doi: 10.1016/j.tecto.2017.12.012

Waldhauser, F., & Schaff, D. P. (2008). Large-scale relocation of two decades of Northern California seismicity using cross-correlation and double-difference methods. *J. Geophys. Res.*, *113*(B8), B08311. doi: 10.1029/2007JB005479

Wang, C.-y., Wang, C.-H., & Manga, M. (2004). Coseismic release of water from mountains: Evidence from the 1999 (Mw = 7.5) Chi-Chi, Taiwan, earthquake. *Geology*, *32*(9), 769–772. doi: 10.1130/G20753.1

Wei, M., Kaneko, Y., Liu, Y., & McGuire, J. J. (2013). Episodic fault creep events in California controlled by shallow frictional heterogeneity. *Nat. Geosci.*, *6*(7), 566–570. doi: 10.1038/ngeo1835

Wen, Y., Li, Z., Xu, C., Ryder, I., & Bürgmann, R. (2012). Postseismic motion after the 2001 Mw 7.8 Kokoxili earthquake in Tibet observed by InSAR time series. *J. Geophys. Res.*, *117*(B8), B08405. doi: 10.1029/2011JB009043